Langmuir

Article

pubs.acs.org/Langmuir

Instability of Liquid Cu Films on a SiO_2 Substrate

Alejandro G. González,*[†,‡] Javier A. Diez,[†,‡] Yueying Wu,[§] Jason D. Fowlkes,[∥] Philip D. Rack,[∥,§] and Lou Kondic[⊥]

[†]Instituto de Física Arroyo Seco, Universidad Nacional del Centro de la Provincia de Buenos Aires, Tandil, Argentina

[‡]CIFICEN-CONICET, Tandil, Argentina

[§]Department of Materials Science and Engineering, University of Tennessee, Knoxville, Tennessee, United States

[∥]Center for Nanophase Materials Sciences, Oak Ridge National Laboratory, Tennessee, United States, and

[⊥]Department of Mathematical Sciences, New Jersey Institute of Technology, Newark, New Jersey, United States

ABSTRACT: We study the instability of nanometric Cu thin films on SiO_2 substrates. The metal is melted by means of laser pulses for some tens of nanoseconds, and during the liquid lifetime, the free surface destabilizes, leading to the formation of holes at first and then in later stages of the instability to metal drops on the substrate. By analyzing the Fourier transforms of the SEM (scanning electron microscope) images obtained at different stages of the metal film evolution, we determine the emerging length scales at relevant stages of the instability development. The results are then discussed within the framework of a long-wave model. We find that the results may differ whether early or final stages of the instability are considered. On the basis of the interpretation of the experimental results, we discuss the influence of the parameters describing the interaction of the liquid metal with the solid substrate. By considering both the dependence of dominant length scales on the film thickness and the measured contact angle, we isolate a model which predicts well the trends found in the experimental data.

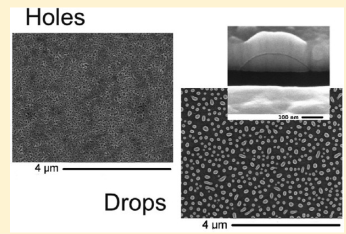

INTRODUCTION

Instabilities of thin liquid films deposited on solid substrates have attracted significant interest for a number of years. These instabilities are important in numerous applications, in particular in the fast growing field of nanofluidics. They lead to the formation of drops, which in the case of liquefied metals, solidify into particles, which find its relevance in applications that range from plasmonics to liquid crystal displays and solar cells;[1−3] for example, the size and distribution of metallic particles is known to be related to plasmon-coupling with incident energy, that has a huge potential of increasing the yield in solar cell devices.[4] To make future progress of relevance to these and other applications, it is important to understand the basic mechanism driving the instabilities.

Stability of a thin film on nanoscale have been extensively studied in the case of polymer films, see, for instance, the recent review by Jacobs et al.[5] However, metal films liquefied by laser irradiation have been considered to a much smaller extent. Instabilities of Cu, Au, and Ni films were considered experimentally,[6] and more recently both experimental and theoretical analyses of dewetting of Co, Ag, Fe, and Ni films have been carried out.[3,7−9] In our earlier works, we have considered instabilities of other liquid metal structures, such as polygons, lines, and rings.[10−13] While these more complex geometries lead to additional insight regarding the instability development, it is important to analyze carefully the simplest case (uniform films), since some of the basic mechanisms leading to instability in different geometries are related. Therefore, a better understanding of uniform films should help us gain better insight into the instability of more complex structures.

For sufficiently thin metal films, of the thicknesses of few nanometers, there is strong evidence that the developing instability is of spinodal type, i.e., it is caused by growth of surface perturbations due to destabilizing effect of liquefied metal/substrate interaction forces.[7,11] The instability evolution proceeds typically by the formation of holes in the liquid metal surface, and a network of connected bridges. The rupture of these bridges lead to a pattern of drops which solidify to form isolated metal particles. The emerging length scales—the distances between holes and/or drops/particles—can then be compared to theoretical models expected to govern the evolution of the described process. How to carry out this comparison is not always clear—for example, one needs to decide which stage of the instability development is to be used. A most obvious question is whether the distances between the holes that form in the initial stages of the instability, or the distances between the drops/particles that remain at the later times are to be considered. To our knowledge, this issue has not been analyzed carefully in the literature so far. This is not surprising, since the evolution happens on a very fast time scale, and it is difficult to capture its properties. We will discuss this topic extensively in the present work and study to which degree the results are influenced by the temporal evolution of the available data.

Received: March 15, 2013
Revised: June 22, 2013
Published: June 27, 2013

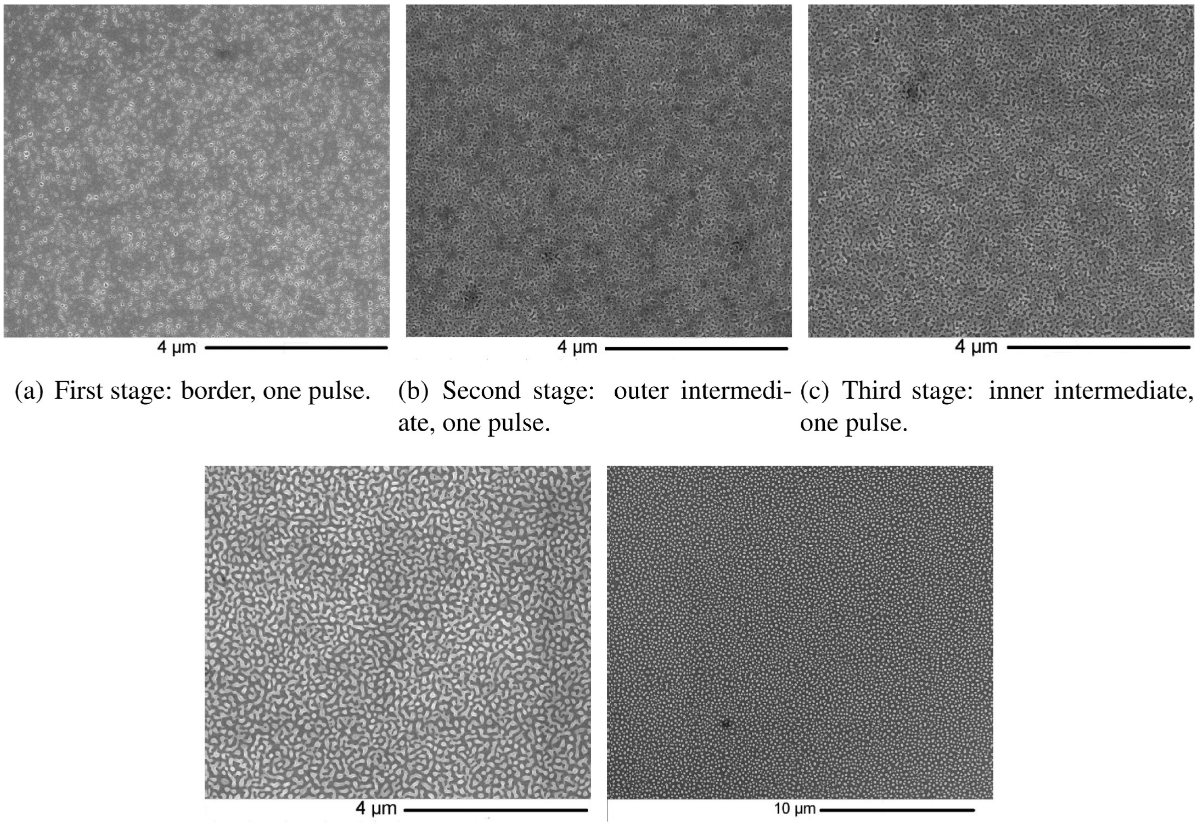

(a) First stage: border, one pulse. (b) Second stage: outer intermediate, one pulse. (c) Third stage: inner intermediate, one pulse.

(d) Fourth stage: center, one pulse. (e) Last stage: center, two pulses.

Figure 1. SEM images of various regions of an 8.0-nm thick Cu film on a SiO_2 substrate. The position of each picture with respect to the center of the laser beam decreases from (a) to (d), and thus the corresponding liquid lifetime increases. Picture (e) is also central as (d), but the film has been irradiated with an extra pulse, and therefore it corresponds to the largest lifetime.

This work centers on experimental and theoretical analysis of Cu films on SiO_2 substrate exposed to laser irradiation. By considering the parts of the experimental domain exposed to different irradiance, we are able to reach some understanding regarding the time evolution of the instability, and therefore distinguish between different stages of its development. The Fourier spectrum of the film thickness allows us to define in a precise manner the emerging wavelengths and, in addition, their time evolution. We should note here that the data analysis that we carry out for the purpose of quantifying the instability development is significantly different from the one which was required for polymer films, due to the difference in the type of the available data. On the one hand, the domain sizes that can be used when liquid metals are considered is orders of magnitude larger than the typical instability wavelength, so that very good statistics can be obtained. This is in contrast to polymer films where domain size is typically a single order of magnitude larger than the typical wavelength, thus reducing the quality of the information that can be reached based on Fourier spectra, and requiring additional methods for data analysis, e.g. based on Minkowski functionals.[5] On the other hand, the evolution in the case of metal films happens much faster (on nanosecond time scales) due to different material properties, and partially for this reason, precise information about temporal evolution of instability is rarely available.

After carrying out Fourier spectra-based analysis of the experimental data, we consider the application of a long-wave (LW) model for the purpose of studying the instability development. One has to be careful regarding the choice of information that is being used: in particular, we find that one obtains different results when holes or drops are considered. Note that previous works have usually considered drops, since they are easier to study and correspond to a fully developed final stage. However, there is no clear evidence whether the experimental data obtained for drops could be reliably related to existing linear theories or not. Therefore, we discuss to which degree the LW model within its linear regime can be used in conjunction with experimental data to extract the material properties entering the governing model, such as the Hamaker constant. Furthermore, we consider different models describing liquid metal/solid substrate interaction and discuss to how the choice of a model influences the results.

■ EXPERIMENTAL SECTION

Copper thin films with thickness ranging from 4.8 to 15.5 nm were sputter deposited onto 100 nm SiO_2 coated silicon chips[14] using radio frequency (RF) magnetron sources. The sputtering conditions are as follows: 5 cm diameter sputter Cu targets and a RF power of 30 W (148 V self-bias), 25 sccm Ar at 5 mTorr processing pressure. The Cu film thickness was measured via optical reflectometry (Filmetrics F20–UV thin-film analyzer).

The films were irradiated in air by either a single or multiple pulses using a normal incident laser beam (~12 mm × 12 mm) that impinges at the center of the sample. The KrF laser has a wavelength of 248 nm and a Gaussian temporal profile whose width (full-width-at-half-maximum) is ~18 ns. The laser energy density was chosen to be 140 mJ/cm^2 to ensure the films reach melting threshold based on the numerical simulation method used in our earlier work.[13] The total fluency of energy received by the metal in a particular region during its irradiation determines the liquid lifetime. Since the laser energy has a Gaussian spatial profile, the decreasing energy density from the center to the edge of the thin films leads to different liquid lifetimes at different regions. This effect allows us to capture information at different stages of the evolution of the liquid film dewetting within a single pulse. Therefore, a region in the center of the pulse has longer liquid lifetime than the regions at the borders. The regions subject to lower fluency can be correlated to early dewetting stages, while those at higher fluency, as well as those irradiated with more pulses, have longer lifetimes and then correspond to later stages.

In contrast to the dewetting process of polymeric films where the dynamic evolution is readily accessible, since it takes place in time scales of the order of seconds, minutes, or even hours, the liquid metal thin films typically require nanoseconds and hence capturing experimentally different dewetting stages is a complex challenge. To this end, nanosecond laser irradiation with a gradient energy distribution provides an effective way to freeze different stages corresponding to different liquid life times. Therefore, it is meaningful to explore the change in experimental length scales during morphology evolution considering different regions, and determine which stage corresponds more closely to existing theoretical models and yields a better estimate of the Hamaker constant.

The morphologies of different stages of the evolution are captured by taking scanning electron microscopy (SEM) images after each pulse of the resolidified sample. In order to have a roughly consistent localization of the energy profile on the thin film after each laser pulse, we align the substrate at practically the same laser position. In this way, we are able to capture different dewetting stages as ones moves from the center to the edge.

Figure 1 shows a typical case of the series of SEM pictures obtained in experiments for Cu films with a thickness of h = 8.0 nm on SiO_2. Figure 1a−d corresponds to pictures taken at the border of the central region of the irradiated sample in a single laser pulse. In Figure 1a, we observe a rather non-uniform distribution of holes which becomes more uniform in Figure 1b. As one considers a region closer to the center of the pulse, the holes become bigger and tend to coalesce, forming a net of rims. In Figure 1d, the rims break up and retract leading to a new configuration which after a second pulse ends up in a distribution of drops (Figure 1e). In summary, this type of analysis of the SEM's allows us to correlate both the position of a picture with respect to the center of the pulse (and/or the number of pulses) with a time sequence that describes the evolution of the film instability.

We have repeated the procedure in a series of 26 experiments with thickness varying from 4.8 nm to as high as 17 nm. We took an average of four pictures for each experiment corresponding to different stages. These images were used to compute the results given in the following section.

Measurement of Contact Angles. We now proceed to measure the static contact angles of the drops resulting after a large number of pulses. We have used two methods. The first one consists in applying a sufficient number of laser pulses to ensure fully developed drops shape. The fluence is controlled and limited in order to minimize evaporation. Examples of these drops are shown in Figure 2a, where the approximating spheres and the calculated contact angles are also shown. The distribution of these angles with respect to drop volumes is shown in Figure 2b for drops obtained from films of different thicknesses. We observe a significant variation of θ for smaller drops ($V < 3 \times 10^{-3}$ μm^3), while the mean value $\langle\theta\rangle$ vary from 69° to 80°. We note that a possible dependence of contact angle on the drop size is an interesting question, which we leave for future work. For the present purposes, the mean values are sufficient.

A drawback of the method described above is that it is difficult to determine the points of contact at the base of a solidified drop, particularly the smaller ones. Therefore, we have also explored an alternative approach that enhances the contrast of the surface of a particle. To do so, we sputtered a thick layer of Ni (~150 nm) on top of Cu drops, and then we milled them by means of a focused ion beam (FIB). This milling process was done with an FEI Nova 600 dual beam scanning electron microscope (SEM) with a gallium ion source under an accelerating voltage of 30 KeV. The ion milling area was defined to

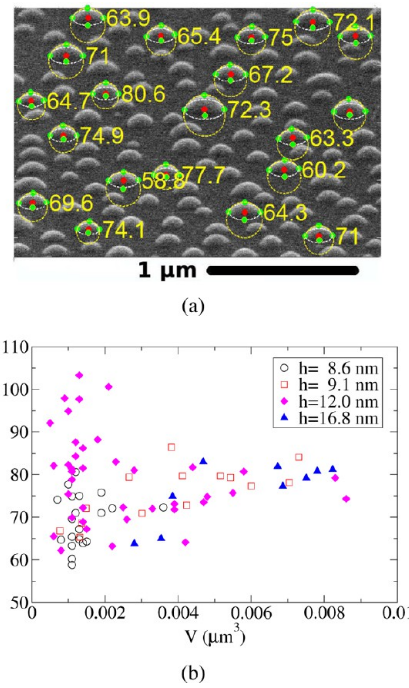

Figure 2. (a) Measurement of contact angles in a sample of solidified drops (particles) resulting from a film of thickness h = 8.7 nm. (b) Distribution of contact angles from films of different thickness, h, versus the drops volume.

show the whole drop cross section (~800 nm × 800 nm area in this case) and was carefully aligned through the center of the particle. After ion milling of each drop, cross section SEM images were taken to determine the contact angle as shown in Figure 3. As a result, the average contact angle of a total of 15 drops is 65° with a standard deviation of 6.9°. This result is consistent with the one given above, suggesting that despite relatively large standard deviations, contact angle is a well-defined quantity on the scales considered.

■ EVOLUTION OF THE INSTABILITY

In order to study the characteristic length scales of the patterns formed by the thin films instability, we have computed the fast Fourier transforms (FFT) of pictures corresponding to different stages of the evolution. For the reasons described in the next paragraph, we consider four subregions of 512 × 512 pixels at the corners of each picture (whose size is 2048 × 1764 pixels), and obtain the corresponding FFTs. First, we verify that there is no preferred direction in the film pattern. Figure 4 shows the density of the transform for a typical subregion. The annular white zone confirms that the distribution of length scales is isotropic. We have verified that isotropic distribution holds for all considered experimental images.

Once confirmed that the FFTs are isotropic, we compute (for each of the four subregions) the radial spectral distribution of wavenumbers, k, by averaging the FFTs over all directions for annuli between k and $k + \delta k$. A good overlapping of the spectra for all four subregions guarantees that the whole picture corresponds to the same stage. Figure 5 shows that this is indeed the case, and therefore we conclude that each of the pictures shown in Figure 1 corresponds to a fairly uniform laser irradiation, and have endured the same liquid lifetime. The peaks of the spectra can be correlated to typical lengths, $l = 2\pi/k$, which, depending on the stage under study, characterize the sizes and distances between holes or drops.

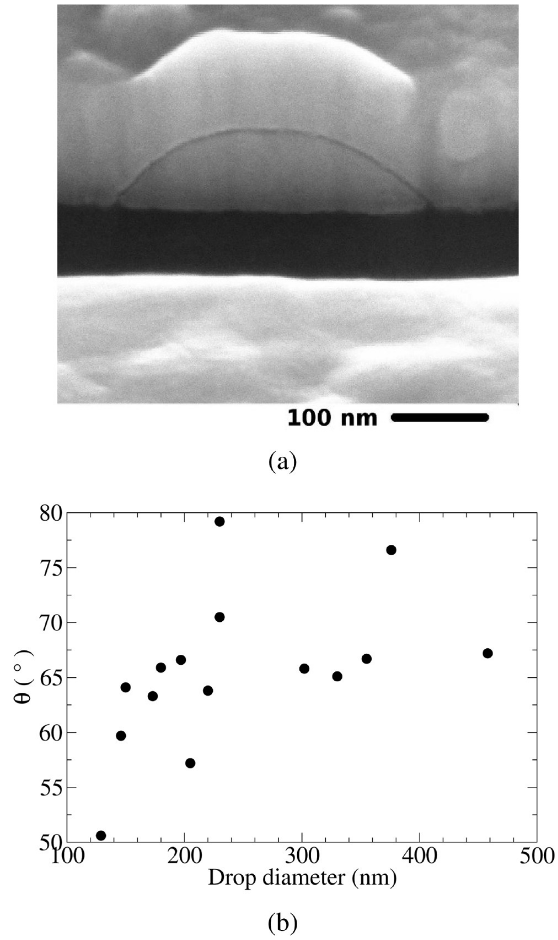

Figure 3. (a) Image of a solidified Cu drop covered with nickel and viewed with a 52° tilt. (b) Distribution of contact angles for different drops versus their projected diameters.

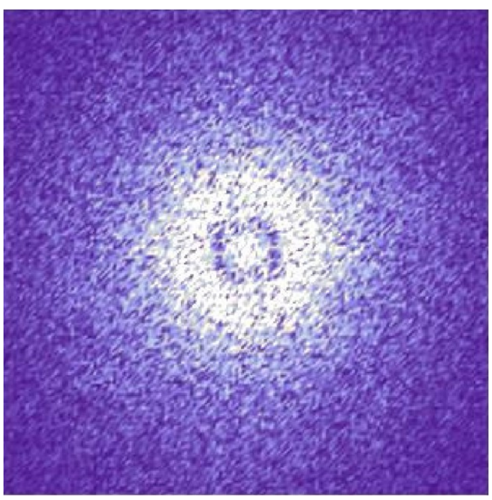

Figure 4. Density plot of the FFT of Figure 1c.

In order to describe the evolution of the film instability, we must correlate the average radial spectra of a picture with a time sequence. For instance, in Figure 1a there is a rather random pattern of holes, and so its average spectra has a weak and wide peak at $k_{max} \approx 100\ \mu m^{-1}$ ($l_{max} \approx 63$ nm) as shown in Figure 5a. This indicates that there is no clear dominant length in this very early stage. The apparent peak around $k = 0$ is an artifact of the method due to the finite size of the sample, and it is more pronounced in the early stages where there are rather extensive connected flat areas. Figure 5b shows instead a spectra with a clear peak at $k_{max} \approx 63\ \mu m^{-1}$ ($l_{max} \approx 100$ nm) in correspondence with the more uniform distribution of holes in Figure 1b. This peak is due to the fact that there is a better defined spacing between holes. In the next stage, the holes are growing and coalescing, thus leading to an increase in the characteristic spacing as seen in the peak at $k_{max} \approx 50\ \mu m^{-1}$ ($l_{max} \approx 125$ nm) in Figure 5c. At the fourth stage in Figure 1d, the bridges and rims around the holes have broken up and have given place to a filament-like structure whose spectra is shown in Figure 5d. This figure shows a narrower peak at a lower wavenumber $k_{max} \approx 38\ \mu m^{-1}$ ($l_{max} \approx 166$ nm). As these elongated structures further contract and break up, a rather uniform distribution of drops shows up (see Figure 1e). The spectrum shown in Figure 5e has a peak at $k_{max} \approx 25\ \mu m^{-1}$ ($l_{max} \approx 250$ nm), thus indicating the final drop spacing. The shape of these drops is very similar to spherical caps, and their average radius contributes to the formation of an incipient secondary peak in the spectra, as seen in Figure 5e for $k \approx 69\ \mu m^{-1}$ ($l \approx 90$ nm).

A typical evolution of these spacings is shown in Figure 6a. Since the total liquid lifetime is not exactly known, we sort the lengths according to the stages, shown in Figure 1, providing therefore a rough idea of the time evolution. The tendency of the pattern to increase its typical length scale is clearly visible. The error in the determination of the distances is calculated from the dispersion of the corresponding k's obtained for each of the four subregions.

We find it useful to separate the evolution into four main stages:

1. a *preliminary early stage*, where no well-defined peak is observed in its spectrum;
2. a *developed early stage*, where the holes distribution is characterized by a clear peak;
3. a series of *intermediate stages*, where bridge breakups and coalescence are produced; and
4. a *final stage*, where drops are clearly visible and characterized by a narrow peak in the spectrum.

The first length scale, l_{max}, which appears in the evolution corresponds to the *developed early stage*, and it characterizes the distance between the centers of the holes formed in the film. We denote such length as l_{holes}. Similarly, when the instability saturates to a final pattern of drops, l_{max} corresponds to the average distance between drop centers, which we call l_{drops} (see Figure 6b).

While analyzing the information from more than 450 spectra, we have found consistently a monotonic increase of l_{max} as we progress from the early second stage to the advanced fourth one above. Therefore, by studying the early second stage (when the thin film linear instability is fully developed, but not affected by nonlinear effects or other types of instability) and the fourth stage (when the drops are completely formed), we cover the full range of emerging length scales. Furthermore, intermediate stages are conceptually complicated to consider since they involve coupling of linear and nonlinear effects. For these reasons, we concentrate on the developed early stage and on the final stage in what follows.

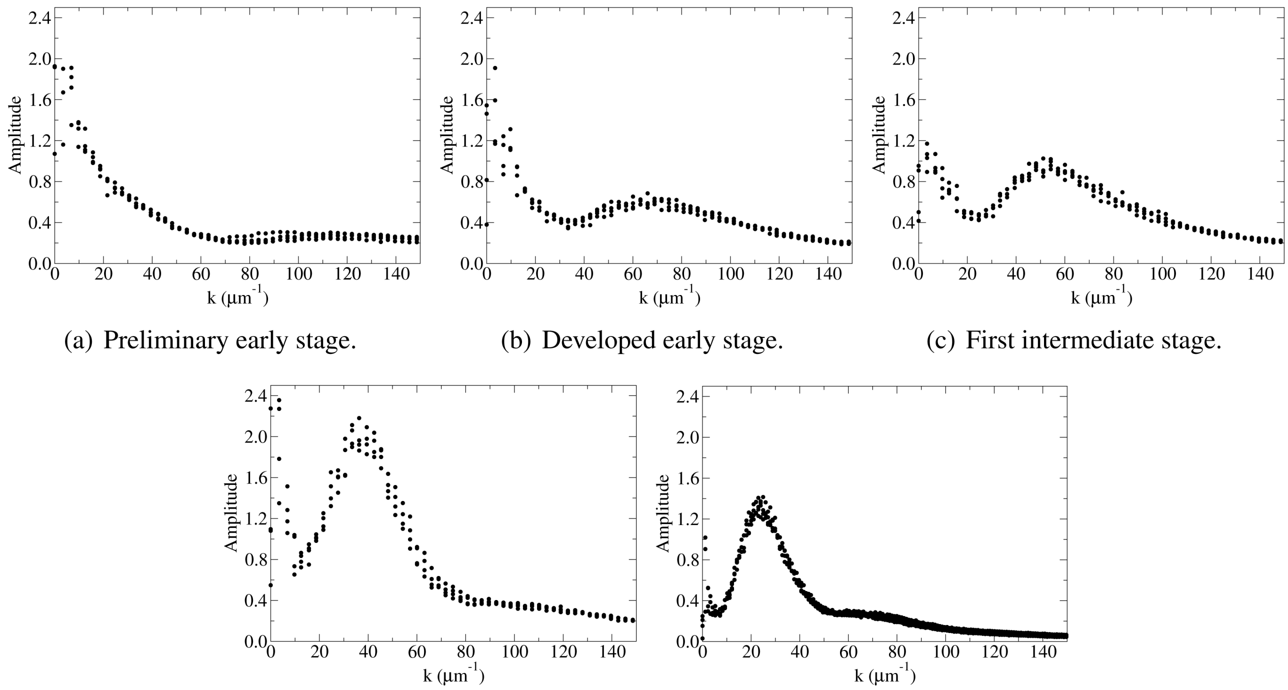

(a) Preliminary early stage. (b) Developed early stage. (c) First intermediate stage.

(d) Second intermediate stage. (e) Last stage.

Figure 5. FFT spectra of the experimental images shown in Figure 1. Each part shows four FFT spectra computed from four subdomains of the experimental images. All of the spectra are plotted with the same symbol. The overlap shows that the patterns in each experimental part belong to the same stage of the evolution. The exposure time increases from (a) to (e).

■ MODELING OF THE INSTABILITY

The typical length scales obtained from the spectra discussed in the previous section are analyzed within the framework of the linear thin film instability under the LW model. In this approach, it is assumed that the flow is driven by both surface tension and van der Waals forces. The latter are described by the so-called disjoining pressure, Π, whose dependence on thickness h involves the competition between long- and short-range forces.[15] While the exact function form of Π is not known, in particular for liquid metals[11,16] (see these references for further discussion), a commonly used expression is as follows:[17−19]

$$\Pi(h) = \kappa\left[\left(\frac{h_*}{h}\right)^n - \left(\frac{h_*}{h}\right)^m\right] \tag{1}$$

where h is the fluid thickness, $n > m$ are positive exponents, and h_* is the equilibrium thickness where repulsive and attractive forces balance. Within the present context, the second term includes the electronic component.[20] The pressure scale, κ, is related to the Hamaker constant, A, as follows:

$$A = 6\pi\kappa h_*^3 \tag{2}$$

Only a small subset of exponents (n,m) has been considered in previous works. It is difficult to obtain them from very first principles, except using additional simplifying assumptions that cannot always be taken for granted in liquid metal films subject to laser irradiation. Typical examples found in the literature[21] considering polymeric films are as follows: (9,3), (4,3), and (3,2). For liquid metals, some of these exponents have been used, and both simplified versions with attractive forces only,[3,7,8] and more complex models with additional exponential term[22] have been implemented.

Since it is unclear from the literature which exponents should be used, in the present work we will explore whether a simple model, specified by eq 1, with (commonly used) sets of exponents provides consistent results, and/or whether one could identify the pair which provides a good agreement with the experimental results for Cu, while remembering that the functional form specified by eq 1 is an approximation itself. Another approximation—the use of the LW model for a problem where equilibrium contact angles are large—should be recalled as well. We expect that this approach is applicable in particular when considering initial stages of instability (leading to hole formation) since during most of the instability development the slopes of the film surface are not too large.

Using this disjoining pressure within the LW model, the wavelength of the mode of maximum growth rate obtained from the linear stability analysis (LSA) is given by the following:[23]

$$\lambda_m = 2\pi\Big/\sqrt{\frac{A}{12\pi\gamma h h_*^3}\left[m\left(\frac{h_*}{h}\right)^m - n\left(\frac{h_*}{h}\right)^n\right]} \tag{3}$$

where γ is the liquid surface tension. Since this formula refers to the linear regime, it is appropriate to assume that λ_m should be related to l_{holes}, although it is frequently found in the literature that it is related to l_{drops} (as well). We also consider this possibility and discuss its implications in an appropriate section below. Here, we proceed to discuss the basic framework which can be used to compare the experimental results to the predictions of the model leading to eq 3. We note that typical values of h_* are estimated in the theories that describe the intermolecular interactions, such as those using Lennard-Jones potentials, and they suggest h_* of the order of a few Å.[24]

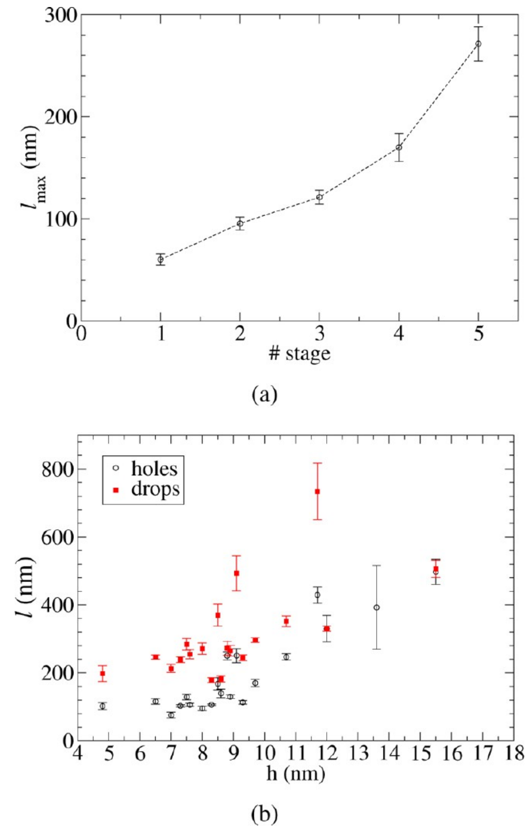

Figure 6. (a) Evolution of the characteristic spacing of the patterns, l_{max} for the experimental images shown in Figure 1. The horizontal axis indicates the numbering of the stage. (b) Average distance between holes (l_{holes}) at the *developed early stage* and drops (l_{drops}) at the *final stage* for different film thickness, h.

To proceed, we first study in some detail the behavior of eq 3 with respect to the exponents (n,m). It is convenient to rewrite this equation as follows:

$$\lambda_m = \sqrt{\frac{48\pi^2\gamma}{mA}h^{m+1}h_*^{3-m}\left[1 - \frac{n}{m}\left(\frac{h_*}{h}\right)^{n-m}\right]^{-1}} \tag{4}$$

Since $h_* \ll h$ for the considered experiments, the square bracket is approximately equal to unity, and consequently λ_m becomes independent of the exponent n, which accounts for the repulsive force term in eq 1. Moreover, for $m = 3$, the dependence on h_* also disappears, and we have the following:

$$\lambda_m = \sqrt{\frac{16\pi^3\gamma}{A}}h^2, \quad \text{for } m = 3 \tag{5}$$

which is an expression frequently used in the literature,[7,8,25] albeit for different metals. For $m \neq 3$, the functional dependence of λ_m on both h and h_* is modified. In particular, for $m = 2$ as, for instance, in the commonly used pair (3,2), we have the following:

$$\lambda_m = \sqrt{\frac{24\pi^3\gamma}{A}}h^{3/2}h_*^{1/2}, \quad \text{for } m = 2 \tag{6}$$

Regarding the time scales involved in the problem, the LSA gives,

$$\tau = \frac{3\mu}{16\gamma\pi^4}\frac{\lambda_m^4}{h^3} \tag{7}$$

where μ is the fluid viscosity. Thus, we have,

$$\tau = \frac{48\pi^2\gamma\mu}{A^2}h^5, \quad \text{for } m = 3 \tag{8}$$

and

$$\tau = \frac{108\pi^2\gamma\mu}{A^2}h_*^2h^3, \quad \text{for } m = 2 \tag{9}$$

Note that $m = 2$ case retains the dependence on h_* unlike the $m = 3$ case, and this implies that the instability develops much faster for the pair (3,2) than for pairs such as (9,3) and (4,3), since $h_* \ll h$.

The static contact angle, θ, of the drops resulting from the instability process can be related to the parameters κ and h_* of the disjoining pressure by the following:[23]

$$\kappa = \frac{\gamma}{2Mh_*}\tan^2\theta \tag{10}$$

where $M = (n - m)/((m - 1)(n - 1))$. Note that here we are assuming the dependence on θ in the form of $(\tan^2\theta)/2$ instead of $(1 - \cos\theta)$, since the former dependence[23,26] results from the linearized form of the free surface curvature,[27] consistently with the hypothesis of small slope in the LW model, while the latter is derived from the complete (nonlinear) form. By using eq 2, we can now express θ in terms of the Hamaker constant, A, and the equilibrium thickness, h_*,

$$\tan\theta = \sqrt{\frac{MA}{3\pi\gamma h_*^2}} \tag{11}$$

In the next two sections we proceed to discuss the utility of the outlined expressions for λ_m and θ for the purpose of explaining the experimental results.

■ ANALYSIS BASED ON THE DISTANCES BETWEEN HOLES

The early stages of the thin film instability, for which the LSA is appropriate, yields as immediate consequence to the formation of holes. Since during a considerable part of this hole formation process the slopes of the film surface are not large, the LW model should accurately describe the dynamics. The process leading to drop formation is much more complex. Therefore, we consider the distance between holes first.

Since one expects that l_{holes} is basically given by λ_m as predicted by the LSA within the LW model, we attempt to fit the experimental values of l_{holes} with eq 3. To do so, we start by choosing two pairs of exponents (9,3) and (4,3), and a value of $h_* = 0.1$ nm that is consistent with the underlying theories. Figure 7 shows that the fittings with both pairs are very similar, which according to eq 2 yield $A = 1.36 \times 10^{-16}$ J. This value is significantly larger than that reported by Eichenlaub et al.,[28,29] which vary between a theoretically calculated value of $A_{calc} = 1.67 \times 10^{-19}$ J and an experimentally measured one of $A_{exp} = 1.42 \times 10^{-19}$ J. One may wonder whether the assumed value of h_* is too small; however, even for h_* as large as 2 nm or so, too high values of A are obtained. Even if Eichenlaub's deductions are disregarded, the values of the Hamaker constant obtained using the pairs of exponents (9,3) and (4,3) are too large to be acceptable in comparison to other results reported in the

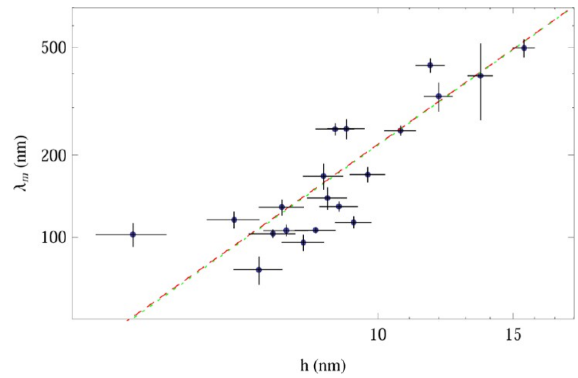

Figure 7. Fitting of l_{holes} (symbols) with λ_m for $h_* = 0.1$ nm. Both exponents (9,3) (dotted line) and (4,3) (dashed line) yield $A = 1.36 \times 10^{-16}$ J.

literature.[3,9,30] Note also h_* of the order of a few nanometers is inconsistent with the underlying molecular models. These results suggest that $m = 3$ for any usual $n > m$ does not lead to acceptable values of A for the considered experimental case of Cu on SiO_2 substrate; it is possible that different metals and/or different substrates may lead to a different conclusion.

Next, we consider $m = 2$ and, in particular, the pair (3,2) which has also been suggested in the literature. Figure 8 shows

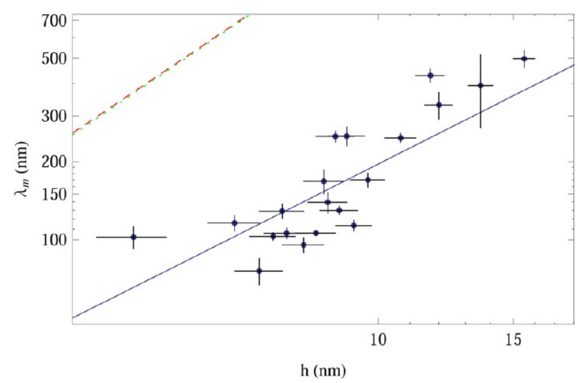

Figure 8. Fitting of l_{holes} (symbols) with λ_m for $h_* = 0.1$ nm. The exponents (3,2) (solid line) yield $A = 2.58 \times 10^{-18}$ J, while (4,3) (dashed line) and (9,3) (dotted line) are unable to fit the data.

the results for $h_* = 0.1$ nm (solid line) which leads to $A = 2.58 \times 10^{-18}$ J. This value, although still larger than those reported by Eichenlaub et al.,[28,29] is 2 orders of magnitude smaller than the one obtained for $m = 3$, and furthermore it is comparable to other results reported in the literature.[3,9,30] Figure 8 also shows that, as expected, the exponents (9,3) and (4,3) for this value of A cannot be used to fit the experimental data (dashed and dotted lines in Figure 8).

We note that the fitting of l_{holes} versus h with eq 6 for λ_m is obtained for a given value of the ratio A/h_*, provided $h_* \ll h$. In fact, we find an approximately linear relationship between the values of A obtained by varying h_* and using the full expression for λ_m, eq 4 (symbols in Figure 9a). The small departure with respect to the average straight line $A = 2.89 \times 10^{-17} h_*$ J, with h_* in nm, is due to the additional term with $n = 3$. This result implies that in order to obtain A as small as 10^{-19} J, one needs to consider $h_* \approx 0.01$ nm, which is unacceptably small from the physical point of view.

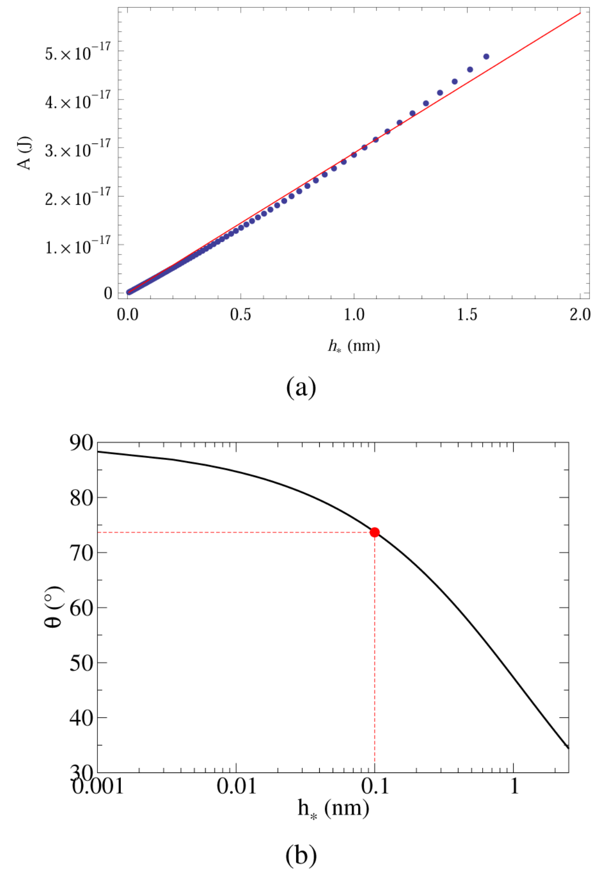

Figure 9. (a) Hamaker constant, A, versus h_* from the fitting of l_{holes} with λ_m. The solid line shows an average linear relationship. (b) Contact angle, θ, versus h_* for (3,2). The symbol on the curve corresponds to the predicted contact angle for $h_* = 0.1$ nm ($\theta = 72.8°$).

Finally, by using a linear approximation for the relation between A and h_* for (3,2) in eq 11, we can relate θ with h_* as shown in Figure 9b. For $h_* = 0.1$ nm, eq 11 yields $\theta = 72.8°$, which is in reasonable agreement with the measured contact angles (see Figures 2 and 3). This can be interpreted as a further confirmation of the selection of exponents (3,2), since the theory gives theoretical angles that are in correspondence with independently measured ones.

We note that several factors may contribute to yield a Hamaker constant larger than that reported by Eichenlaub et al.[29] The studies based on Lifshitz theory,[24] have demonstrated that van der Waals or Casimir forces can be modified due to a change of the optical properties of the materials.[31−38] This change can be produced by the generation of extra free electrons due to the laser irradiation, which may take place in our case in both metal and Si under the 100 nm SiO_2 layer. For instance, under an irradiation of a 1.7 ns (full width half-maximum) laser with an effective energy of 30 μJ and a photon energy of 3.68 eV, Inui[37] reported an increase of Casimir force between two 100 nm thick Si plates with a separation of 1 μm of about 1.5 times the force without laser irradiation. In our case, the free carrier generation rate under the laser pulse energy of 0.14 J/cm^2 can reach above 10^{16}−10^{17} cm^{-3} per nanosecond, and hence a modified dielectric constant is expected. As for the metal film, modified dielectric constant and nonlinear optical response under ultrafast laser irradiation have been widely explored.[39−41] Bigot et al.[42] used an 80 fs pump laser with a maximum pump energy density of 0.5 mJ/ cm^2 to investigate the effect of interband and intraband transition on optical properties of Cu nanoparticles. With a modified energy status distribution due to an increase of electron temperature[39] and enhancement of Fermi energy as a result of interband transitions, as well as a different inverse collision time of the collective mode, it is showed that the corresponding dielectric constant can be modified by the laser excitation. Comparing the laser energy density used by Bigot et al. (6×10^{-6} J/fs cm^2) to the laser energy density applied in our experiment ($\sim 8 \times 10^{-6}$ J/fs cm^2), a similar phenomenon may take place in our Cu film while the laser duration is much longer than a femtosecond laser. Besides the laser effect, an increased temperature that may smear the electronic distribution around the Fermi energy can also modify the liquid metal optical constant. This brief discussion provides only some of the possibilities that may lead to an increase of the actual Hamaker constant. Further work is needed to understand how relevant any of these effects actually is.

ANALYSIS BASED ON THE DISTANCES BETWEEN DROPS

The distance between drops, l_{drops}, has been also considered in determining the characteristic length scale of the instability, despite the fact that drops are the outcome of complex dynamics which is not necessarily well described (if at all) by the linear stability analysis. Still, we consider drops as well in order to illustrate the differences in the results when considering drops versus holes. Figure 10 shows the distance

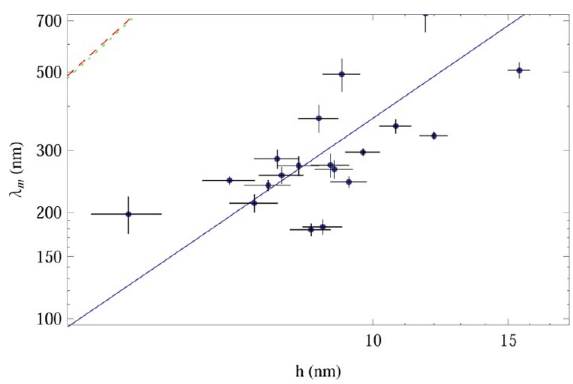

Figure 10. Fitting of l_{drops} (symbols) with λ_m for $h_* = 0.1$ nm. The exponents (3,2) (solid line) yield $A = 2.58 \times 10^{-18}$ J, while (4,3) (dashed line) and (9,3) (dotted line) do not provide good fits for this value of A.

between the drops, and corresponding fits obtained using eq 3 for $h_* = 0.1$ nm, and the same pairs of exponents as in previous section. Due to the larger dispersion of the experimental results, the linear regression in the log−log plot in the figure is not as good as that for l_{holes}; for instance, the standard deviation of the data with respect to the fit is now almost twice as large. Nevertheless, the pair (3,2) still yields a reasonable fit for l_{drops}, while pairs such as (9,3) and (4,3) lead to fitting lines which do not describe the experimental results well. The (3,2) pair leads to the best fit for a Hamaker constant $A = 7.18 \times 10^{-19}$ J, which is smaller than the one obtained with l_{holes}, and it is coincidentally closer to the reported values.[28] However, following a similar procedure as the one described in the previous section to calculate the contact angle, we find $\theta =$ 59.7°, which is out of the range of the measured angles (see Figure 2b and Figure 3b). As discussed previously, this finding is not surprising due to the complexity of nonlinear effects which are responsible for the drop formation.

The failure to get a good fit for drops, and the reasonable results for holes, is not so surprising if one takes into account that the considered model is based on the linear stability analysis, and therefore small perturbations from a base state (flat film). Furthermore, one also cannot expect a good agreement with the theory by considering intermediate stages of instability, since during these stages nonlinear effects already become dominant. The intermediate stages can provide interesting information about growth rates, mixing of instabilities or evolution to a nonlinear regime, but these studies will require further extensive analysis that is out of the scope of the present work.

CONCLUSIONS

In this work, we have considered the evolution of the instability of Cu films on SiO_2 substrates, where the metal is liquefied by exposure to laser irradiation. One distinguishing feature of this study is that, by analyzing regions of the film exposed to different levels of irradiation, we are able to define several stages of the instability development. When considering initial stages, we find a clear signature of the spinodal type of instability manifesting itself in a well-defined peak in the Fourier spectrum, and thus suggesting the existence of a length scale that characterizes the emerging features. The experimental results are then analyzed using a long-wave (LW) model. The wavelength of maximum growth rate as given by the linear stability analysis performed within this model allows us to extract the values of the Hamaker constant describing the liquid metal/solid substrate interaction. The values thus obtained are found to be larger than expected based on the (limited) available literature, but consistent with other works considering similar systems. We find that the functional form of the disjoining pressure model describing liquid/solid interaction has a strong influence on the comparison between the experiment and the theory; only one of the usual exponent pairs defining the disjoining pressure can provide a reasonable fit to the experimental results. Furthermore, significantly different results are found when the model is applied to the drops/particles (which are formed in the last stages of the instability development and do not change their shape with additional laser pulses) instead of holes that form during early stages. This suggests that much care is required when applying the tools of LW (or any other) theory for the purpose of understanding the experimental data: the conclusions may be sensitive to the properties of the considered model, as well as to the choice of the time at which the experimental data are extracted. For example, the standard results regarding scaling of the emerging length and time scales with the film thickness, h, do depend on the parameters entering the model. For the present study of Cu films on SiO_2 substrates, we find that the exponent pair (3,2) provides a good agreement for the scaling of the wavelength, λ, with h, ($\lambda \approx h^{3/2}$), while the other pairs of exponents, leading to $\lambda \approx h^2$, do not provide accurate description of the experimental data, at least for the system considered here.

The results given in this work show that linear stability analysis of the underlying LW model, when used carefully, can be utilized for developing an accurate description of the experimental data. We expect that these results will bring us a step closer in developing better understanding of the instability evolution in other, more complex liquid metal geometries. This will be a subject of our future work.

■ AUTHOR INFORMATION

Corresponding Author

*E-mail: aggonzal@exa.unicen.edu.ar.

Notes

The authors declare no competing financial interest.

■ ACKNOWLEDGMENTS

P.D.R. and L.K. acknowledge partial support by the NSF Grants No. CBET 1235651 and 1235710, respectively. A portion of this work was conducted at the Center for Nanophase Materials Sciences, which is sponsored at Oak Ridge National Laboratory by the Scientific User Facilities Division, Office of Basic Energy Sciences, U.S. Department of Energy. A.G.G. and J.A.D. acknowledge support from Consejo Nacional de Investigaciones Cientificas y Técnicas de la República Argentina (CONICET, Argentina) with Grant PIP 844/2011 and visits to ORNL with a joint CONICET-NSF international cooperation project.

■ REFERENCES

(1) Maier, S. A.; Kik, P. G.; Atwater, H. A.; Meltzer, S.; Harel, E.; Koel, B. E.; Requicha, A. A. Local detection of electromagnetic energy transport below the diffraction limit in metal nanoparticle plasmon waveguide. *Nat. Matter.* **2003**, *2*, 229–232.

(2) Sun, S.; Murray, C.; Weller, D.; Folks, L.; Moser, A. Monodisperse FePt nanoparticles and ferromagnetic FePt nanocrystal superlattices. *Science* **2000**, *287*, 1989–1992.

(3) Krishna, H.; Shirato, N.; Favazza, C.; Kalyanaraman, R. Energy driven self-organization in nanoscale metallic liquid films. *Phys. Chem. Chem. Phys.* **2009**, *11*, 8136–8143.

(4) Maier, S. *Plasmonics: Fundamentals and Applications*; Springer-Verlag: New York, 2007.

(5) Jacobs, K.; Herminghaus, S.; Seemann, R. In *Thin Liquid Films*; Tsui, O., Russel, T., Eds.; World Scientific: Hackensack, NJ, 2008; p 243.

(6) Herminghaus, S.; Jacobs, K.; Mecke, K.; Bischof, J.; Fery, A.; Ibn-Elhaj, M.; Schlagowski, S. Spinodal dewetting in liquid crystal and liquid metal films. *Science* **1998**, *282*, 916–919.

(7) Favazza, C.; Kalyanaraman, R.; Sureshkumar, R. Robust nanopatterning by laser-induced dewetting of metal nanofilms. *Nanotechnology* **2006**, *17*, 4229–4234.

(8) Trice, J.; Thomas, D.; Favazza, C.; Sureshkumar, R.; Kalyanaraman, R. *Phys. Rev. Lett.* **2008**, *101*, 017802.

(9) McKeown, J. T.; Roberts, N. A.; Fowlkes, J. D.; Wu, Y.; LaGrange, T.; Reed, B. W.; Campbell, G. H.; Rack, P. D. Real-time observation of nanosecond liquid-phase assembly of nickel nanoparticles via pulsed-laser heating. *Langmuir* **2012**, *28*, 17168–17175.

(10) Kondic, L.; Diez, J.; Rack, P.; Guan, Y.; Fowlkes, J. Nanoparticle assembly via the dewetting of patterned thin metal lines: Understanding the instability mechanism. *Phys. Rev. E* **2009**, *79*, 026302.

(11) Wu, Y.; Fowlkes, J. D.; Rack, P. D.; Diez, J. A.; Kondic, L. On the breakup of patterned nanoscale copper rings into droplets via pulsed-laser-induced dewetting: competing liquid-phase instability and transport mechanisms. *Langmuir* **2010**, *26*, 11972–11979.

(12) Wu, Y.; Fowlkes, J. D.; Roberts, N. A.; Diez, J. A.; Kondic, L.; González, A. G.; Rack, P. D. Competing liquid phase instabilities during pulsed laser induced self-assembly of copper rings into ordered nanoparticle arrays on SiO_2. *Langmuir* **2011**, *27*, 13314.

(13) Fowlkes, J. D.; Kondic, L.; Diez, J.; Rack, P. D. Self-assembly versus directed assembly of nanoparticles via pulsed laser induced dewetting of patterned metal films. *Nano Lett.* **2011**, *11*, 2478–2485.

(14) Klein, K.; Melechko, A.; Rack, P.; Fowlkes, J.; Meyer, H.; Simpson, M. Cu–Ni composition gradient for the catalytic synthesis of vertically aligned carbon nanofibers. *Carbon* **2005**, *43*, 1857–1863.

(15) Seemann, R.; Herminghaus, S.; Jacobs, K. Dewetting patterns and molecular forces: a reconciliation. *Phys. Rev. Lett.* **2001**, *86*, 5534.

(16) Ajaev, V.; Willis, D. Thermocapillary flow and rupture in films of molten metal on a substrate. *Phys. Fluids* **2003**, *15*, 3144.

(17) Mitlin, V. S. On dewetting conditions. *Colloids Surf.* **1994**, *89*, 97–101.

(18) Schwartz, L. W. Hysteretic effects in droplet motion on heterogenous substrates: Direct numerical simulation. *Langmuir* **1998**, *14*, 3440.

(19) Mitlin, V. Dewetting revisited: New asymtotics of the film stability diagram and the metastable regime of nucleation and growth of dry zones. *J. Colloid Interface Sci.* **2000**, *227*, 371–379.

(20) Derjaguin, B.; Leonov, L.; Roldughin, V. Disjoining pressure in liquid metallic films. *J. Colloid Interface Sci.* **1985**, *108*, 207–214.

(21) Craster, R. V.; Matar, O. K. Dynamics and stability of thin liquid films. *Rev. Mod. Phys.* **2009**, *81*, 1131–1198.

(22) Krishna, H.; Sachan, R.; Strader, J.; Favazza, C.; Khenner, M.; Kalyanaraman, R. Thickness-dependent spontaneous dewetting morphology of ultrathin Ag films. *Nanotechnology* **2010**, *21*, 155601.

(23) Diez, J.; Kondic, L. On the breakup of fluid films of finite and infinite extent. *Phys. Fluids* **2007**, *19*, 072107.

(24) Israelachvili, J. N. *Intermolecular and Surface Forces*, second ed.; Academic Press: New York, 1992.

(25) Trice, J.; Thomas, D.; Favazza, C.; Sureshkumar, R.; Kalyanaraman, R. Pulsed-laser-induced dewetting in nanoscopic metal films: Theory and experiments. *Phys. Rev. B* **2007**, *75*, 235439.

(26) Schwartz, L.; Eley, R. Simulation of droplet motion on low-energy and heterogeneous surfaces. *J. Colloid Interface Sci.* **1998**, *202*, 173.

(27) Münch, A.; Wagner, B. Contact-line instability of dewetting thin films. *Physica D* **2005**, *209*, 178–190.

(28) Butt, H.-J.; Kappl, M. *Surface and Interfacial Forces*; Wiley-VCH Verlag: Weinheim, 2010.

(29) Eichenlaub, S.; Chan, C.; Beaudoin, S. P. Hamaker constants in integrated circuit metalization. *J. Colloid Interface Sci.* **2002**, *248*, 389–397.

(30) Shirato, N.; Krishna, H.; Kalyanaraman, R. Thermodynamic modeling for the dewetting instability in ultra thin films. *J. Appl. Phys.* **2010**, *108*, 024313.

(31) Chen, F.; Klimchitskaya, G. L.; Mostepanenko, V. M.; Mohideen, U. Control of the Casimir force by the modification of dielectric properties with light. *Phys. Rev. B* **2007**, *76*, 035338.

(32) Chan, H. B.; Bao, Y.; Zou, J.; Cirelli, R. A.; Klemens, F.; Mansfield, W. M.; Pai, C. S. Measurement of the Casimir force between a gold sphere and a silicon surface with nanoscale trench arrays. *Phys. Rev. Lett.* **2008**, *101*, 030401.

(33) Bao, Y.; Guérout, R.; Lussange, J.; Lambrecht, A.; Cirelli, R. A.; Klemens, F.; Mansfield, W. M.; Pai, C. S.; Chan, H. B. Casimir force on a surface with shallow nanoscale corrugations: Geometry and finite conductivity effects. *Phys. Rev. Lett.* **2010**, *105*, 250402.

(34) Klimchitskaya, G. L.; Mohideen, U.; Mostepanenko, V. M. The Casimir force between real materials: Experiment and theory. *Rev. Mod. Phys.* **2009**, *81*, 1827–1885.

(35) Arnold, W.; Hunklinger, S.; Dransfeld, K. Influence of optical absorption on the Van der Waals interaction between solids. *Phys. Rev. B* **1979**, *19*, 6049–6056.

(36) Klimchitskaya, G. L. Normal and lateral Casimir force: Advances and prospects. *J. Phys.: Conf. Ser.* **2010**, *258*, 012001.

(37) Inui, N. Change in the Casimir force between semiconductive bodies by irradiation. *J. Phys.: Conf. Ser.* **2007**, *89*, 012018.

(38) Vogel, T.; Dodel, G.; Holzhauer, E.; Salzmann, H.; Theurer, A. High-speed switching of far-infrared radiation by photoionization in a semiconductor. *Appl. Opt.* **1992**, *31*, 329–337.

(39) Shirato, N.; Krishna, H.; Kalyanaraman, R. Ultrafast nonlinear mirrors with broad spectral and angular bandwidths in the visible spectral range. *Opt. Express* **2013**, *21*, 3573–3581.

(40) Hopkins, P. E. Influence of inter- and intraband transitions to electron temperature decay in noble metals after short pulsed laser heating. *J. Heat Transfer* **2010**, *132*, 122402.
(41) Voisin, C.; Del Fatti, N.; Christofilos, D.; Vallée, F. Ultrafast electron dynamics and optical nonlinearities in metal nanoparticles. *J. Phys. Chem. B* **2001**, *105*, 2264−2280; *Phys. Rev. Lett.* **1995**, *75*, 4702.
(42) Bigot, J. Y.; Merle, J. Y.; Cregut, O.; Daunois, A. Electron dynamics in copper metallic nanoparticles probed with femtosecond optical pulses. *Phys. Rev. Lett.* **1995**, *75*, 4702−4705.